

Conductivity control via minimally invasive anti-Frenkel defects in a functional oxide




Donald M. Evans, Theodor S. Holstad, Aleksander B. Mosberg, Didrik R. Småbråten, Per Erik Vullum, Anup L. Dadlani, Konstantin Shapovalov, Zewu Yan, Edith Bourret, David Gao, Jaakko Akola, Jan Torgersen, Antonius T. J. van Helvoort, Sverre M. Selbach, Dennis Meier

Angaben zur Veröffentlichung / Publication details:

Evans, Donald M., Theodor S. Holstad, Aleksander B. Mosberg, Didrik R. Småbråten, Per Erik Vullum, Anup L. Dadlani, Konstantin Shapovalov, et al. 2020. "Conductivity control via minimally invasive anti-Frenkel defects in a functional oxide." *Nature Materials* 19 (11): 1195–1200. <https://doi.org/10.1038/s41563-020-0765-x>.



Conductivity control via minimally invasive anti-Frenkel defects in a functional oxide

Donald M. Evans^{1,10}  , Theodor S. Holstad^{1,10}, Aleksander B. Mosberg^{2,10} , Didrik R. Småbråten^{1,10} , Per Erik Vullum³, Anup L. Dadlani⁴ , Konstantin Shapovalov⁵, Zewu Yan^{6,7}, Edith Bourret⁷, David Gao^{2,8}, Jaakko Akola^{2,9}, Jan Torgersen⁴ , Antonius T. J. van Helvoort², Sverre M. Selbach¹  and Dennis Meier¹  

Utilizing quantum effects in complex oxides, such as magnetism, multiferroicity and superconductivity, requires atomic-level control of the material's structure and composition. In contrast, the continuous conductivity changes that enable artificial oxide-based synapses and multiconfigurational devices are driven by redox reactions and domain reconfigurations, which entail long-range ionic migration and changes in stoichiometry or structure. Although both concepts hold great technological potential, combined applications seem difficult due to the mutually exclusive requirements. Here we demonstrate a route to overcome this limitation by controlling the conductivity in the functional oxide hexagonal Er(Mn,Ti)O₃ by using conductive atomic force microscopy to generate electric-field induced anti-Frenkel defects, that is, charge-neutral interstitial-vacancy pairs. These defects are generated with nanoscale spatial precision to locally enhance the electronic hopping conductivity by orders of magnitude without disturbing the ferroelectric order. We explain the non-volatile effects using density functional theory and discuss its universality, suggesting an alternative dimension to functional oxides and the development of multifunctional devices for next-generation nanotechnology.

A continuous range of conductivity levels in oxide materials can enable innovative technologies, such as multilevel data storage in memristor chips and synaptic devices for neuromorphic computing^{1–4}. Different mechanisms^{5,6} are now established that allow for tuning the conductivity in oxides gradually and by multiple orders of magnitude⁷. For example, electric fields modify the n-type conductivity in LaAlO₃-SrTiO₃ heterostructures⁸ and multiferroic BiFeO₃ thin films⁹, which has been explained based on the creation and migration of positively charged oxygen vacancies (V_O[•]). In addition, migration of negatively charged oxygen interstitials (O_i[•]) has been exploited to control the p-type conductivity in hexagonal Y_{0.67}Lu_{0.33}MnO₃ single crystals¹⁰. However, both the migration of V_O[•] and O_i[•] are aspects of the same phenomenon, that is, an electric-field-driven redox reaction of a transition metal oxide. Although these redox reactions give the desired conductivity changes, the creation of either V_O[•] or O_i[•] necessarily also alters the overall stoichiometry in the host material, with a substantial impact on the material's spin, charge and orbital degrees of freedom. The latter is reflected by the sensitivity of oxides towards variations in stoichiometry, which can drive systems between metallic and insulating states¹¹, stabilize superconductivity¹² or completely suppress magnetic¹³ and electric order^{14,15}. In general, the long-range migration and extraction and/or injection of ions associated with the currently applied redox reactions induces a net mass transport that gives rise to chemical, electrostatic and strain-related gradients.^{2,14,16} This prohibits utilization in parallel with emergent electronic functionalities beyond merely conductivity.

To avoid detrimental side effects and ultimately utilize the full range of functional properties available in oxide materials, a conceptually different approach to the control of conductivity is needed. Particularly promising are stoichiometric defects as classically reported, for example, in ionic fluorites¹⁵. Here, anions move from lattice sites to interstitial positions to form entropy-stabilized and charge-neutral interstitial-vacancy pairs (anti-Frenkel defects¹⁵). Although in electroceramics it is clear that intrinsic anti-Frenkel defects play a key role for the ionic–electronic transport, their utilization to control conductivity in correlated oxides remains unexplored. Most studies in the field of oxide electronics focus on systems from the large family of perovskite materials, which are unlikely to form anti-Frenkel defects due to their rather dense crystal structure. As a consequence, fundamental aspects, such as their creation, stability and impact on functionalities other than mixed ionic–electronic transport, fall into largely uncharted territory.

In this study, we work with the ferroelectric p-type semiconductor ErMnO₃ (single crystals (Methods)) from the family of hexagonal manganites with 0.2% Ti doping (denoted h-Er(Mn,Ti)O₃ in the following). The applied Ti doping lowers the conductivity, $\sigma_{dc}(h\text{-Er(Mn,Ti)O}_3) = 2.6 \times 10^{-8} \Omega^{-1} \text{ cm}^{-1}$, compared with $\sigma_{dc}(h\text{-ErMnO}_3) = 2.5 \times 10^{-7} \Omega^{-1} \text{ cm}^{-1}$ for the undoped sample¹⁷. Aside from its semiconducting properties, h-Er(Mn,Ti)O₃ exhibits a spontaneous polarization along its [001] axis ($P \approx 6 \mu\text{C cm}^{-2}$), which emerges at $T_c \approx 1,470 \text{ K}$ driven by a tripling of the structural unit cell^{18–20}. Importantly, the structure of hexagonal manganites is about 11% less dense than the corresponding orthorhombic perovskite

¹Department of Materials Science and Engineering, Norwegian University of Science and Technology (NTNU), Trondheim, Norway. ²Department of Physics, Norwegian University of Science and Technology (NTNU), Trondheim, Norway. ³SINTEF Industry, Trondheim, Norway. ⁴Department of Mechanical and Industrial Engineering, Norwegian University of Science and Technology (NTNU), Trondheim, Norway. ⁵Institut de Ciència de Materials de Barcelona (ICMAB-CSIC), Campus UAB, Bellaterra, Spain. ⁶Department of Physics, ETH Zurich, Zürich, Switzerland. ⁷Materials Sciences Division, Lawrence Berkeley National Laboratory, Berkeley, CA, USA. ⁸Nanolayers Research Computing Ltd, London, UK. ⁹Computational Physics Laboratory, Tampere University, Tampere, Finland. ¹⁰These authors contributed equally: Donald M. Evans, Theodor S. Holstad, Aleksander B. Mosberg, Didrik R. Småbråten. ✉e-mail: donald.evans@ntnu.no; dennis.meier@ntnu.no

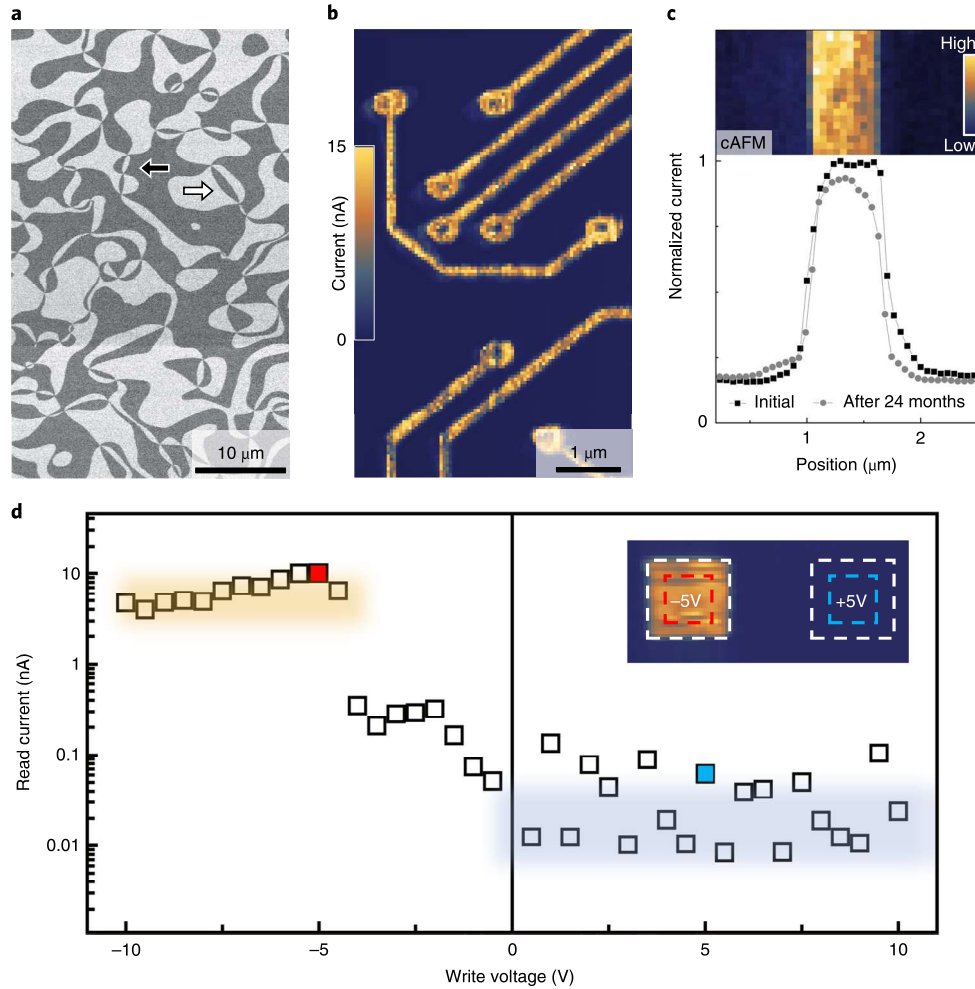


Fig. 1 | Local conductance control in h-Er(Mn,Ti)O₃. **a**, Piezoresponse force microscopy (in-plane contrast) image showing the characteristic distribution of ferroelectric domains. Arrows indicate the polarization direction (dark, $-P$ and bright, $+P$). **b**, cAFM scan showing conducting nanowires (bright) on a less conducting background of both $-P$ and $+P$ domains similar to those in **a**. The image was gained with a positive bias ($U^{\text{read}} = +10$ V) after writing wires with a negative bias of $U^{\text{write}} = -8$ V. Voltages were applied to the back electrode. **c**, Normalized current read on a conducting bar right after writing it on a sample with out-of-plane P and, read again, 24 months later ($U^{\text{read}} = +12$ V, $U^{\text{write}} = -21$ V). The profiles were gained from cAFM images, as shown in the inset, by averaging over multiple cross-sections. The curves are offset so that the background current away from the conducting feature aligns. The data reflect the long-term stability of the electric-field-induced conducting features in h-Er(Mn,Ti)O₃. **d**, Average current measured at $U^{\text{read}} = +10$ V from a series of $1 \times 1 \mu\text{m}^2$ boxes written with voltages between -10 and $+10$ V. Inset: representative spatially resolved cAFM data for boxes written with ± 5 V. The white dashed lines frame the boxes, whereas the coloured dashed lines mark the areas ($0.5 \times 0.5 \mu\text{m}^2$) over which the current is averaged to quantify the read current.

structure, and $V_{\text{O}}^{\cdot\cdot}$ and $\text{O}_i^{\cdot\cdot}$ are equally important for the electronic properties^{21,22}. In addition, such defects are already mobile below 200 °C, whereas cations migrate only above 800 °C, which enables anion-defect-driven electronic property control^{23,24}.

Local control of electrical conductance

Figure 1a presents the distribution of ferroelectric 180° domains in h-Er(Mn,Ti)O₃ acquired by piezoresponse force microscopy on a sample with in-plane P ([110] orientation (Methods)). Figure 1b shows a representative conductance map, gained by conductive atomic force microscopy (cAFM) using a conducting probe tip (curvature radius ~ 100 nm) after writing a network of wires with negative voltage, $U^{\text{write}} = -8$ V, applied to the back electrode. The image was recorded with a positive voltage, $U^{\text{read}} = +10$ V, and shows different wires with a width of about 100 nm and enhanced conductance compared with that of the surrounding material. The effect is equally pronounced in $\pm P$ domains and occurs on surfaces with in-plane P (Fig. 1b) and surfaces with out-of-plane P (Fig. 1c, inset). We note that this is qualitatively different from the

$\text{O}_i^{\cdot\cdot}$ -migration-induced changes in conductance in h-Y_{0.67}Lu_{0.33}MnO₃, which were reported to occur under comparable conditions but only on surfaces with in-plane P (ref. 10). Importantly, we found that the enhanced conductance of our electric-field-induced features persist on the timescale of years under ambient conditions (Fig. 1c), and no signature of degradation was observed up to 105 °C (Supplementary Fig. 1). A reset to the original state is possible by annealing at 300 °C, which reflects a barrier for stability in the order of 0.035–0.050 eV (Supplementary Fig. 2). Furthermore, and in contrast to previous AFM-written conducting nanofeatures in LaAlO₃–SrTiO₃ (refs. 8,25) that rely on hydrogen (H^+) penetration, our structures are robust against solvents, such as acetone, ethanol and methanol. In fact, we did not observe qualitative differences between the writing of conducting features in air (ambient) and under a nitrogen atmosphere (Supplementary Fig. 3), which discards H^+ penetration as the driving force behind the change in conductivity. The conclusion that neither only $\text{O}_i^{\cdot\cdot}$ nor only H^+ is responsible for the enhanced conductance is corroborated by time- and voltage-dependent studies (Supplementary Fig. 4), as well as by local transport measurements

(Supplementary Fig. 5), which cannot be explained by only one type of defect. To quantify the induced changes in conductivity and to analyse the influence of the polarity (+ or –) and size of the applied voltage, we drew a series of boxes (Fig. 1d, inset) and systematically varied the write voltage U^{write} from –10 V to +10 V. The impact of the varying U^{write} was monitored by a cAFM scan taken with a positive voltage of +10 V. The results are summarized in Fig. 1d, which shows the averaged measured current, I^{read} , as a function of U^{write} . Figure 1d reveals that I^{read} depends on the polarity of the write voltage: for negative voltages that exceeded –5 V, we observed an increase in the conductance by about three orders of magnitude. In contrast, positive voltages did not lead to an increase in the conductance, consistent with the formation of a Schottky barrier at the tip-sample interface.^{10,26} The latter was also confirmed by separate experiments at higher voltages up to +60 V (Supplementary Fig. 6). Thus, the experiments demonstrate that conducting features can be written with negative voltages ($U^{\text{write}} \lesssim -5$ V) and read-out by positive voltages ($0 < U^{\text{read}} \lesssim +60$ V). By writing features of different shapes (wires and dots), we achieved an enhancement of up to four orders of magnitude in I^{read} without substantial changes in surface topography (Supplementary Figs. 7 and 8). The data demonstrate that localized electric fields can enhance the conductance in h-Er(Mn,Ti)O₃ by up to four orders of magnitude; the changes are durable, resistant to moderate heating and chemical solvents, and can be induced with a nanometre spatial precision.

Three-dimensional morphology and structural properties

To understand the origin of the enhanced conductance, we investigated how the effect evolved within the bulk. Figure 2a and inset show a comparison of scanning electron microscopy (SEM) and cAFM images from the same area, which reveals an elliptically shaped bright area that was written with $U^{\text{write}} = -60$ V applied for 5 s. A comparison of the SEM and cAFM data shows that the bright contrast in SEM correlates with a high conductance. This correlation allows us to evaluate how the electric-field-induced changes protrude into the depth of the sample based on SEM images. For this purpose, we took cross-sectional images from the region of interest (Fig. 2b) using a dual-beam focused ion beam (FIB) (Methods). Consistent with our AFM data (Supplementary Fig. 8), the cross-sectional SEM images show no notable change in surface topography. Instead, Fig. 2b reveals that the region of enhanced conductance extends more than 0.5 μm into the depth of the sample. A schematic 3D reconstruction of the conducting area based on the SEM data is presented in Fig. 2c. This distribution is consistent with the anisotropic behaviour observed in the electronic transport²⁷ and ionic mobility in the hexagonal manganites (Supplementary Fig. 9), which indicates that the changes that give rise to an enhanced conductance are a bulk phenomenon rather than a surface effect.

To test for related structural modifications in the bulk, we took high-angle annular dark-field scanning transmission electron microscopy (HAADF-STEM) lattice images inside and away from the conducting region shown in Fig. 2b. Figure 2d,e presents HAADF-STEM scans viewed down the [100] direction to compare the electrically modified region to the as-grown structure, respectively. The images represent the typical up–up–down pattern of Er atoms²⁸, separated by layers of Mn atoms. Interestingly, both real and reciprocal space investigations show no differences in positions between the two regions (Fig. 2d,e and insets, and Supplementary Fig. 10). In particular, when we analysed the arrangement of Er atoms, we found no statistically significant differences in Er displacement within the conductive region or modification of the unit cell size, which suggests that the driving mechanism for enhanced conductivity is due to subtle effects related to the local electronic structure. Furthermore, as the improper electric polarization in h-Er(Mn,Ti)O₃ arises from the Er displacement^{29–32}, its robustness demonstrates that the orientation and magnitude of the ferroelectric

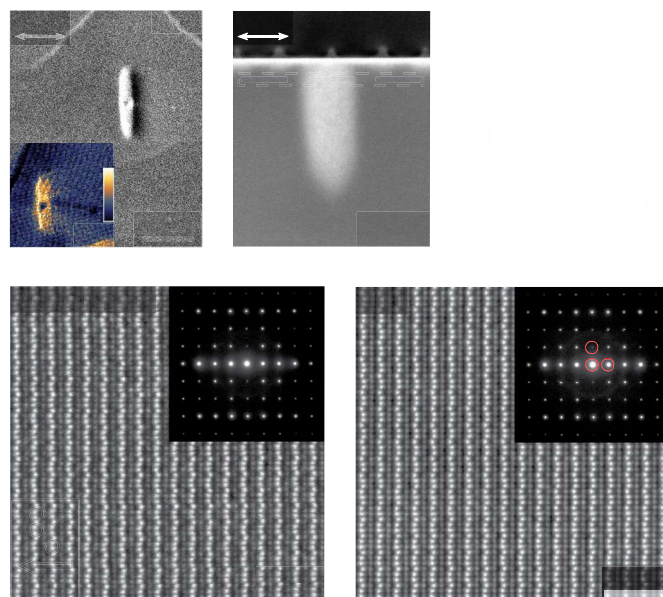


Fig. 2 | Morphology and structure of electric-field-induced conducting features. **a**, Top-down SEM and cAFM (inset, $U^{\text{read}} = +45$ V) images of an elliptically shaped conducting region (bright) generated by applying $U^{\text{write}} = -60$ V for 5 s with the probe tip kept stationary. The white arrow indicates the ferroelectric axis ($P \parallel \langle 001 \rangle$). **b**, SEM image of a FIB cross-section from **a** that reveals how the conducting feature protrudes into the bulk of h-Er(Mn,Ti)O₃ and shows where, in the final transmission electron microscopy (TEM) lamella, the EELS line scan for Fig. 3 was taken (blue and yellow represent the bulk and electrically modified region, respectively). **c**, 3D sketch representing the cAFM-induced conducting feature and the shape dependence on the crystallographic axes based on the cross-section in **b** and cross-sections of equivalent dots taken in perpendicular directions. **d**, HAADF-STEM image from the conductive region seen in **b**, viewed along the $P6_3cm$ [100] zone axis. The brighter Er atomic positions show the characteristic up–up–down displacement as discussed in Holtz et al.²⁹ and the arrow in the bottom inset shows how this links to the ferroelectric polarization P . Top inset: corresponding selected area electron diffraction pattern. **e**, HAADF-STEM image taken in the unmodified bulk region viewed as for **d**. Inset: corresponding selected area electron diffraction pattern. The analysis of the crystal lattice in **d**, **e** and Supplementary Fig. 10 reveals no measurable differences, which reflects that the atomic-scale structure and, hence, the ferroelectric polarization, are unaffected by the electric-field-induced change in conductivity.

order is unaffected by the electric-field-induced increase in conductance (Fig. 2a,b).

Electrochemical structure and electric-field-induced modifications

We next analyse the electronic structure at the local scale, using electron energy-loss spectroscopy (EELS). Figure 3a displays averaged EELS spectra, which show the Mn $L_{2,3}$ -edge in the bulk (blue) and in the modified conducting region (yellow). A comparison of the EELS data reveals changes in spectral weight, whereas the L_3/L_2 white-line-intensity ratio remains constant, which suggests that the net Mn oxidation state is preserved. We demonstrated the reproducibility of this subtle effect by recording EELS spectra at the Mn $L_{2,3}$ -edge from a second line scan in different positions, which led to qualitatively equivalent results (Supplementary Fig. 11). To evaluate the detected change, we followed an approach used in the literature^{33–37} and fitted the full Mn $L_{2,3}$ -edge with three spectra, which corresponded to Mn²⁺ and Mn⁴⁺ spectra³⁷ and experimental

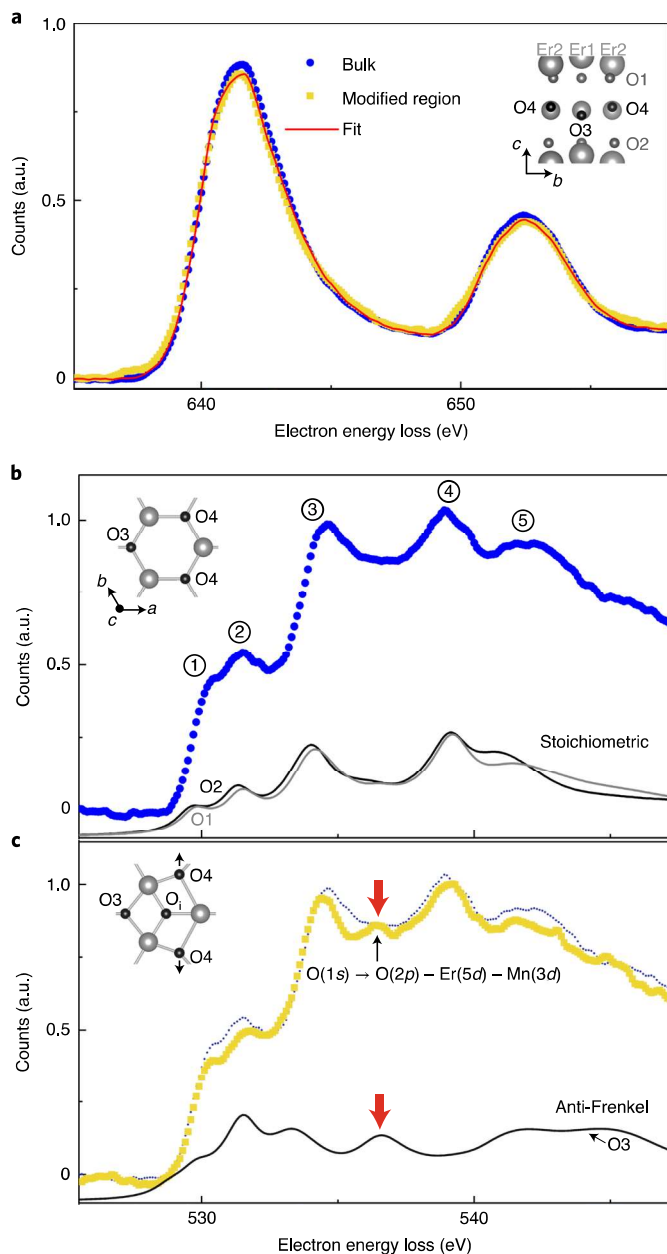


Fig. 3 | Comparison of the electronic structure in as-grown and electrically modified regions. **a**, Blue and yellow data points represent EELS spectra of the Mn $L_{2,3}$ -edge in h-Er(Mn,Ti)O₃ taken in the bulk and in the modified conducting region, respectively (ratio of lamella thickness (t) and mean free path (λ), $t/\lambda = 0.40 \pm 0.02$). The red line is a fit to the Mn $L_{2,3}$ -edge in the conducting region based on a linear combination of spectra that correspond to Mn²⁺, Mn³⁺ and Mn⁴⁺ valence states with 3.75% Mn²⁺ and 3.75% Mn⁴⁺, that is, approximately one anti-Frenkel defect in every nine unit cells. Inset: symmetry-inequivalent Er and O positions. **b**, Data points present the O K-edge in the bulk. Grey and black lines are calculated spectra for apical oxygen (O1 and O2), respectively, in a stoichiometric crystal. **c**, Yellow points present the O K-edge in the region with enhanced conductivity (the bulk spectrum (blue) is shown for reference). The black line is the calculated spectrum for planar oxygen (O3) in the presence of anti-Frenkel defects, as sketched in the inset. Transitions are labelled according to the projected DOS (Supplementary Fig. 13b). Red arrows indicate a peak at about 537 eV, which is characteristic for contributions from planar oxygen. All the EELS spectra were taken on the same single line scan with an even sample thickness and are spatially averaged over the regions indicated by the blue and yellow lines in Fig. 2b. a.u., arbitrary units.

reference spectra recorded away from the conducting region. This procedure allowed us to quantify relative changes with respect to the bulk even without knowing the exact defect density in the as-grown state (note that bulk h-Er(Mn,Ti)O₃ displays a p-type conductivity, which implies the presence of O_i^{••} (Supplementary Fig. 5)). We found that linear combinations of two spectra (bulk and Mn²⁺, or bulk and Mn⁴⁺) alter the peak form and $L_{3/2}$ white-line-intensity ratio, which makes it unlikely that only one defect type (either V_O^{••} or O_i^{••}) is responsible for the experimentally observed change in spectral weight (see Supplementary Figs. 11 and 12 for details). In contrast, assuming an equal concentration of Mn²⁺ and Mn⁴⁺, we reproduced the averaged EELS spectra for the Mn $L_{2,3}$ -edge in the conducting regime (red lines in Fig. 3a and Supplementary Fig. 11), which suggests a coexistence of V_O^{••} and O_i^{••}. The latter is consistent with the formation of (V_O^{••}, O_i^{••}) defect pairs, that is, anti-Frenkel defects¹⁵. On the basis of our fits, we calculated an increase of about $3.25 \pm 0.5\%$ in the concentration of Mn⁴⁺ and Mn²⁺ relative to that in the bulk, which corresponds to about one anti-Frenkel defect for every nine unit cells (Supplementary Fig. 12).

To find additional evidence, we considered EELS spectra taken at the O K-edge in the bulk (Fig. 3b) and in the conducting region (Fig. 3c) and applied the ab initio self-consistent multiple-scattering code FEFF³⁸ to analyse emergent site-specific differences for the four symmetrically inequivalent oxygen positions¹⁹ in h-Er(Mn,Ti)O₃ (Fig. 3a, inset). Representative calculated spectra for apical (O1 and O2) and planar (O3) oxygen are given as insets to Fig. 3b,c, respectively. For the bulk, the spectra calculated for apical oxygen in an oxygen stoichiometric system adequately replicate the main features of the O K-edge, labelled 1–5 (an overview of all the oxygen spectra is given in Supplementary Fig. 13). In contrast, in the conducting region (yellow in Fig. 3c) the O K-edge shows several differences compared with that of the bulk, which include the emergence of a distinct peak at about 537 eV, which cannot be explained based on apical oxygen alone. At this energy, however, a peak is present in the calculated spectra for planar oxygen (O3, black line), which is expected to have an increased contribution in the presence of anti-Frenkel defects due to changes in the oxygen bond angle (illustration in the Fig. 3c inset). Although the O K-edge results are in tune with the data gained at the Mn $L_{2,3}$ -edge and consistent with the formation of anti-Frenkel defects, from the spectroscopy data alone one cannot unambiguously conclude a coexistence of both V_O^{••} and O_i^{••}. Direct evidence of this coexistence is provided, however, by the time- and voltage-dependent study in Supplementary Fig. 4, which shows a separation of positively (V_O^{••}) and negatively (O_i^{••}) charged defects under a longer exposure to electric fields.

Stability and electronic properties of anti-Frenkel defects

To develop a microscopic model, we applied first-principles calculations based on density functional theory (DFT) using the isostructural compound h-YMnO₃ as the model system (analogous to Mundy et al.³³, the calculations were performed for h-YMnO₃, which is structurally and electronically similar to h-ErMnO₃, but the absence of f electrons simplifies the DFT description) (Methods). We found that O_i^{••} (locally contracting the lattice²¹) and V_O^{••} (locally expanding the lattice³⁹) are structurally screened and, hence, do not recombine when more than ~ 6 Å apart. Instead, at $T = 0$ K, they form an electrically compensated metastable anti-Frenkel defect (V_O^{••}, O_i^{••}) as sketched in Fig. 4a (see Supplementary Notes 1 and 2, and Supplementary Figs. 14 and 15 for details). These defects cause a change in the electronic density of states (DOS) compared with that of the stoichiometric structure (Fig. 4b) as illustrated in Fig. 4c. To gain insight into the defect structure at finite temperature and analyse its stability, we performed molecular dynamics simulations at 300, 573 and 1,000 K (Supplementary Fig. 16 and Supplementary Note 3). The molecular dynamics simulations reveal that the system can slightly lower its energy by forming O_i^{••} dimers, which

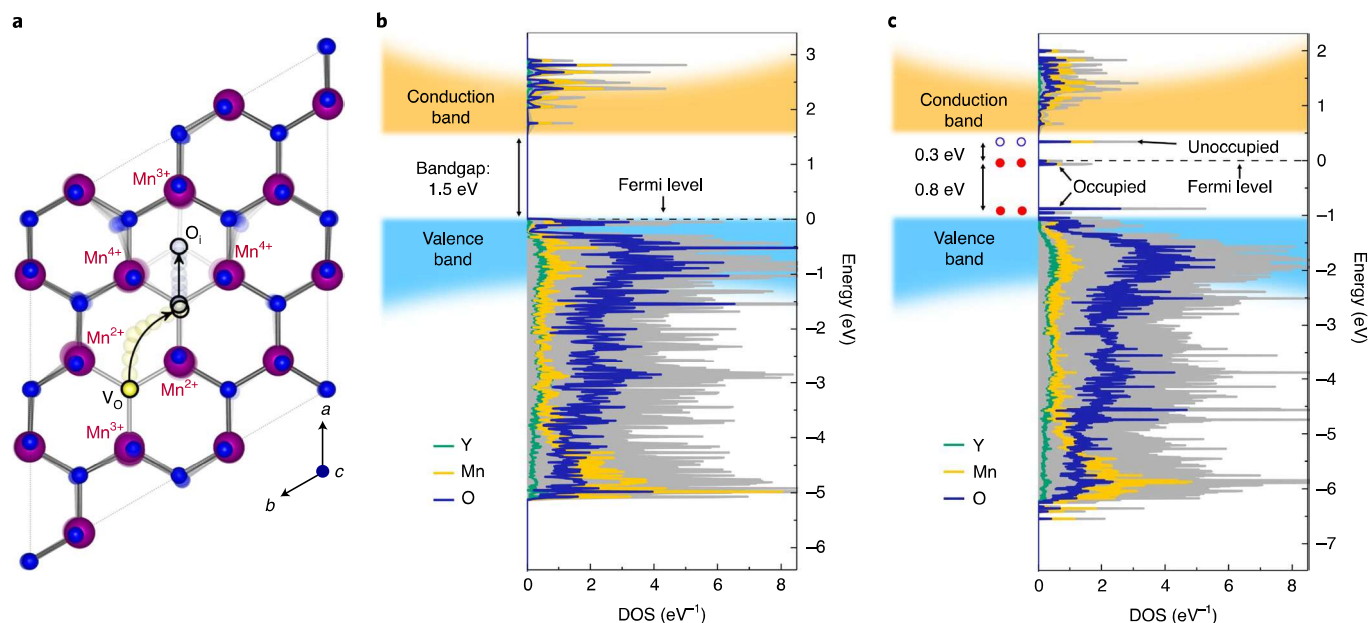


Fig. 4 | Anti-Frenkel defects and electronic DOS. **a**, Formation of an anti-Frenkel defect in a 120-atom supercell. A planar lattice oxygen (yellow) is migrating from its lattice site into another planar oxygen lattice site (grey), which in turn is nudged into an interstitial site, which results in the formation of an anti-Frenkel defect. The resulting local charge compensation of the constituting O_i and V_O are labelled Mn^{4+} and Mn^{2+} , respectively. **b**, Total (grey) and atomic electronic DOS for a stoichiometric 270-atom h-YMnO₃ supercell with key features schematically highlighted. **c**, Same calculation for a 270-atom h-YMnO₃ supercell that contains one anti-Frenkel defect, that is, one anti-Frenkel defect in every nine unit cells or, equivalently, 3.70% Mn atoms in the Mn^{4+} state and 3.70% in the Mn^{2+} state. The red and blue spheres in **c** schematically illustrate the occupied and unoccupied defect states, respectively, within the band gap.

subtly modifies the basic anti-Frenkel defect structure in Fig. 4a (see Supplementary Fig. 16 for an illustration). The modified anti-Frenkel defect exhibits a DOS comparable to that in Fig. 4c and, importantly, does not recombine at 300 and 573 K within 5 and 10 ps trajectories, respectively. In contrast, at 1,000 K we observed recombination within 3 ps, which confirms that recombination occurs at sufficiently high temperature (Supplementary Note 3).

The higher conductance in regions with an enhanced anti-Frenkel defect density can be understood from the calculated electronic DOS and the corresponding simplified band structure shown in Fig. 4c (see Supplementary Fig. 17 for the site-specific DOS). In general, electrical transport in h-Er(Mn,Ti)O₃ occurs via hopping conductivity, reported as Poole–Frenkel conduction¹⁷, and the same mechanism is observed in the modified region (Supplementary Fig. 18). Figure 4c shows that both the number of charge carriers and defect sites available for hopping increase, which explains the observed higher hopping conductivity. The electron–hole pairs associated with anti-Frenkel defects may recombine and give rise to an electrically uncompensated charge state of the anti-Frenkel defect. However, the latter is energetically costly so that new charge carriers would be created to replace the missing electron–hole pair and move the system back to equilibrium (Supplementary Fig. 15).

Outlook

The electric-field-induced anti-Frenkel defects studied in this work enable a minimally invasive and non-volatile conductivity control with nanoscale spatial precision. Importantly, the emergence of parasitic chemical, electrostatic and strain-related gradients associated with conventional approaches is avoided and the material's overall stoichiometry is preserved. Anti-Frenkel defects can be applied in any system that can stably compensate multiple oxygen stoichiometries, such as the families of hexagonal rare-earth gallates and indates⁴⁰, hexaferrite⁴¹, fluorites⁴², Ruddlesden–Popper⁴³ systems and tungsten bronzes. Here—analogue to the hexagonal

manganites—their controlled creation via electric fields is likely, which allows an increase in the density of the defect sites and an enhanced hopping conductivity. With this, a new generation of multifunctional oxides becomes possible in which multilevel conductivity control can be utilized in parallel with phenomena such as ferroelectricity, magnetism and superconductivity without changing the electronic interactions that control them.

Online content

Any methods, additional references, Nature Research reporting summaries, source data, extended data, supplementary information, acknowledgements, peer review information; details of author contributions and competing interests; and statements of data and code availability are available at <https://doi.org/10.1038/s41563-020-0765-x>.

References

- Seok Jeong, D., Kim, I., Ziegler, M. & Kohlstedt, H. Towards artificial neurons and synapses: a materials point of view. *RSC Adv.* **3**, 3169–3183 (2013).
- Ielmini, D. & Wong, H. S. P. In-memory computing with resistive switching devices. *Nat. Electron.* **1**, 333–343 (2018).
- Del Valle, J., Ramírez, J. G., Rozenberg, M. J. & Schuller, I. K. Challenges in materials and devices for resistive-switching-based neuromorphic computing. *J. Appl. Phys.* **124**, 211101 (2018).
- Chanthbouala, A. et al. A ferroelectric memristor. *Nat. Mater.* **11**, 860–864 (2012).
- Hwang, H. Y. et al. Emergent phenomena at oxide interfaces. *Nat. Mater.* **11**, 103–113 (2012).
- Ramesh, R. & Schlom, D. G. Creating emergent phenomena in oxide superlattices. *Nat. Rev. Mater.* **4**, 257–268 (2019).
- Lee, J. S., Lee, S. & Noh, T. W. Resistive switching phenomena: a review of statistical physics approaches. *Appl. Phys. Rev.* **2**, 31303 (2015).
- Cen, C. et al. Nanoscale control of an interfacial metal–insulator transition at room temperature. *Nat. Mater.* **7**, 298–302 (2008).

9. Du, N. et al. Field-driven hopping transport of oxygen vacancies in memristive oxide switches with interface-mediated resistive switching. *Phys. Rev. Appl.* **10**, 54025 (2018).
10. Wang, X. et al. Anisotropic resistance switching in hexagonal manganites. *Phys. Rev. B* **99**, 054106 (2019).
11. Nagarajan, L. et al. A chemically driven insulator–metal transition in non-stoichiometric and amorphous gallium oxide. *Nat. Mater.* **7**, 391–398 (2008).
12. Cava, R. J. et al. Oxygen stoichiometry, superconductivity and normal-state properties of $\text{YBa}_2\text{Cu}_3\text{O}_{7-x}$. *Nature* **329**, 423–425 (1987).
13. Zhao, J. et al. Lattice and magnetic structures of PrFeAsO , $\text{PrFeAsO}_{0.85}\text{F}_{0.15}$, and $\text{PrFeAsO}_{0.85}$. *Phys. Rev. B* **78**, 132504 (2008).
14. Kalinin, S. V., Jesse, S., Tselev, A., Baddorf, A. P. & Balke, N. The role of electrochemical phenomena in scanning probe microscopy of ferroelectric thin films. *ACS Nano* **5**, 5683–5691 (2011).
15. Maier, J. *Physical Chemistry of Ionic Materials: Ions and Electrons in Solids* (Wiley, 2004).
16. Kumar, A., Ciucci, F., Morozovska, A. N., Kalinin, S. V. & Jesse, S. Measuring oxygen reduction/evolution reactions on the nanoscale. *Nat. Chem.* **3**, 707–713 (2011).
17. Holstad, T. S. et al. Electronic bulk and domain wall properties in B-site doped hexagonal ErMnO_3 . *Phys. Rev. B* **97**, 85143 (2018).
18. Chae, S. C. et al. Direct observation of the proliferation of ferroelectric loop domains and vortex–antivortex pairs. *Phys. Rev. Lett.* **108**, 167603 (2012).
19. Van Aken, B. B., Palstra, T. T. M., Filippetti, A. & Spaldin, N. A. The origin of ferroelectricity in magnetoelectric YMnO_3 . *Nat. Mater.* **3**, 164–170 (2004).
20. Han, M.-G. et al. Ferroelectric switching dynamics of topological vortex domains in a hexagonal manganite. *Adv. Mater.* **25**, 2415–2421 (2013).
21. Skjærvø, S. H. et al. Interstitial oxygen as a source of p-type conductivity in hexagonal manganites. *Nat. Commun.* **7**, 13745 (2016).
22. Skjærvø, S. H., Småbråten, D. R., Spaldin, N. A., Tybell, T. & Selbach, S. M. Oxygen vacancies in the bulk and at neutral domain walls in hexagonal YMnO_3 . *Phys. Rev. B* **98**, 184102 (2018).
23. Remsen, S. & Dabrowski, B. Synthesis and oxygen storage capacities of hexagonal $\text{Dy}_{1-x}\text{Y}_x\text{MnO}_{3+\delta}$. *Chem. Mater.* **23**, 3818–3827 (2011).
24. Bergum, K. et al. Synthesis, structure and magnetic properties of nanocrystalline YMnO_3 . *Dalton Trans.* **40**, 7583–7589 (2011).
25. Bi, F. et al. ‘Water-cycle’ mechanism for writing and erasing nanostructures at the $\text{LaAlO}_3/\text{SrTiO}_3$ interface. *Appl. Phys. Lett.* **97**, 173110 (2010).
26. Schaab, J. et al. Electrical half-wave rectification at ferroelectric domain walls. *Nat. Nanotechnol.* **13**, 1028–1034 (2018).
27. Katsufuji, T. et al. Dielectric and magnetic anomalies and spin frustration in hexagonal RMnO_3 ($R = \text{Y}$, Yb , and Lu). *Phys. Rev. B* **64**, 104419 (2001).
28. Zhang, Q. H. et al. Direct observation of interlocked domain walls in hexagonal RMnO_3 ($R = \text{Tm}$, Lu). *Phys. Rev. B* **85**, 20102 (2012).
29. Holtz, M. E. et al. Topological defects in hexagonal manganites: inner structure and emergent electrostatics. *Nano Lett.* **17**, 5883–5890 (2017).
30. Fennie, C. J. & Rabe, K. M. Ferroelectric transition in YMnO_3 from first principles. *Phys. Rev. B* **72**, 100103 (2005).
31. Artyukhin, S., Delaney, K. T., Spaldin, N. A. & Mostovoy, M. Landau theory of topological defects in multiferroic hexagonal manganites. *Nat. Mater.* **13**, 42–49 (2013).
32. Cano, A. Hidden order in hexagonal RMnO_3 multiferroics ($R = \text{Dy}$, Lu , In , Y , and Sc). *Phys. Rev. B* **89**, 214107 (2014).
33. Mundy, J. A. et al. Functional electronic inversion layers at ferroelectric domain walls. *Nat. Mater.* **16**, 622–627 (2017).
34. Tan, H., Verbeeck, J., Abakumov, A. & Van Tendeloo, G. Oxidation state and chemical shift investigation in transition metal oxides by EELS. *Ultramicroscopy* **116**, 24–33 (2012).
35. Nishida, S. et al. Effect of local coordination of Mn on $\text{Mn-L}_{2,3}$ edge electron energy loss spectrum. *J. Appl. Phys.* **114**, 54906 (2013).
36. Loomer, D. B., Al, T. A., Weaver, L. & Cogswell, S. Manganese valence imaging in Mn minerals at the nanoscale using STEM-EELS. *Am. Mineral.* **92**, 72–79 (2007).
37. Garvie, L. A. J. & Craven, A. J. High-resolution parallel electron energy-loss spectroscopy of Mn $\text{L}_{2,3}$ -edges in inorganic manganese compounds. *Phys. Chem. Miner.* **21**, 191–206 (1994).
38. Rehr, J. J., Kas, J. J., Vila, F. D., Prange, M. P. & Jorissen, K. Parameter-free calculations of X-ray spectra with FEFF9. *Phys. Chem. Chem. Phys.* **12**, 5503–5513 (2010).
39. Overton, A. J., Best, J. L., Saratovsky, I. & Hayward, M. A. Influence of topotactic reduction on the structure and magnetism of the multiferroic YMnO_3 . *Chem. Mater.* **21**, 4940–4948 (2009).
40. Griffin, S. M., Reidulff, M., Selbach, S. M. & Spaldin, N. A. Defect chemistry as a crystal structure design parameter: intrinsic point defects and Ga substitution in InMnO_3 . *Chem. Mater.* **29**, 2425–2434 (2017).
41. Zhang, X., Zhang, Y., Yue, Z. & Zhang, J. Influences of sintering atmosphere on the magnetic and electrical properties of barium hexaferrites. *AIP Adv.* **9**, 085129 (2019).
42. Keeton, S. C. & Wilson, W. D. Vacancies, interstitials, and rare gases in fluorite structures. *Phys. Rev. B* **7**, 834–843 (1973).
43. Boulahya, K., Muñoz-Gil, D., Gómez-Herrero, A., Azcondo, M. T. & Amador, U. $\text{Eu}_2\text{SrCo}_{1/3}\text{Fe}_{2/3}\text{O}_7$ a new promising Ruddlesden–Popper member as a cathode component for intermediate temperature solid oxide fuel cells. *J. Mater. Chem. A* **7**, 5601–5611 (2019).

Methods

Samples. High-quality single crystals were grown by the pressurized floating-zone method⁴⁴ and different samples were oriented by Laue diffraction and cut to thicknesses of ~0.5–1 mm. The surfaces were chemomechanically polished with silica slurry to give a root-mean-square roughness of about 1 nm.

Scanning probe microscopy. The scanning probe microscopy measurements were recorded using a NT-MDT NTEGRA Prima scanning probe microscope. For all the cAFM scans presented in the main text, we used TipsNano DCP20 probes with the voltage applied to the back of the sample. For the piezoresponse force microscopy scans we used Asylec-01-R2 Ti/Ir probes with an a.c. voltage amplitude of 10 V applied to the back of the sample.

TEM. TEM specimens were prepared using a Thermo Fisher Scientific G4 UX DualBeam FIB. In situ lift-out was done with backside milling and a final polishing voltage of 2 kV. (S)TEM was performed with a double spherical-aberration corrected cold FEG JEOL ARM 200FC, operated at 200 kV and equipped with a GIF Quantum ER. High-resolution HAADF-STEM images were taken with a spatial resolution of 78 pm. The energy resolution, as determined by the full-width at half-maximum of the zero-loss peak, in EELS was 0.5 eV. HAADF-STEM images were acquired with a beam semiconvergence angle of 27 mrad, inner and outer semicollection angles of 43 and 170 mrad, and a beam current of 22 pA. STEM-EELS acquisitions were performed with a beam current of 120 pA and semicollection angle into the GIF of 33 mrad, combined with 0.05 eV per channel energy dispersion. Dual EELS was performed to realign the energy scale in all the spectra. The EELS data in Fig. 3 were taken in a single 820-nm-long line, which was then split into three 200-nm-wide regions, as indicated in Fig. 2, that were spatially averaged to give the spectra presented in Fig. 3. To measure the Er displacement, a series of fast/short-exposure HAADF-STEM images were acquired and processed with SmartAlign⁴⁵. Atom plane detection was done with Atomap⁴⁶ and averages were computed based on all planes.

DFT. DFT calculations were performed with the projector augmented wave method⁴⁷ as implemented in VASP^{48,49}. $3 \times 3 \times 1$ supercells with 270 atoms are used, with expected $\text{Mn}^{2+}/\text{Mn}^{4+}$ concentrations of 3.70%, to mimic the measured concentrations. For Y, Mn and O, 11, 11 and 6 electrons, respectively, were treated as valence electrons, with a plane-wave energy cutoff of 550 eV. Brillouin zone integration was done on a Γ -centred $1 \times 1 \times 2$ k -point mesh for geometry optimizations, and on a $2 \times 2 \times 3$ mesh for DOS calculations. The DOS calculations have an energy resolution of 0.0067 eV per point. The non-collinear magnetic structure of the Mn sublattice was approximated by a collinear frustrated antiferromagnetic order⁵⁰. Experimental lattice parameters⁵¹ and bandgap⁵² were reproduced using the PBEsol functional⁵³ and spin-polarized GGA+U⁵⁴ with a Hubbard U of 5 eV on Mn $3d$. In defect cells, the ionic positions were optimized under fixed bulk lattice parameters until the forces on all ions were below $0.01 \text{ eV } \text{\AA}^{-1}$. Charge corrections for the charged defects in the periodic boundary conditions were accounted for by extrapolation based on the Madelung potential⁵⁵. As the electronic properties of oxygen stoichiometric¹⁹ and non-stoichiometric^{21,22} hexagonal manganites are governed by the bonding between Mn($3d$) and O($2p$) states, we chose the prototypical h-YMnO₃ as our DFT model system to avoid f electrons and slow convergence with Er.

EELS simulations. A unit cell of 30 atoms was used as the input file in FEFF. Theoretical EELS (on approximately 115-atom clusters) spectra were simulated using the FEFF9 code^{56,57} based on Green's function multiple-scattering theory, in which the parameters SCF (specifies the radius of the cluster for full multiple scattering during the self-consistency loop) and FMS (computes full multiple scattering within a sphere of radius r centred on the absorbing atom) were set to certain values. An SCF of 4 Å, FMS of 6 Å and a corehole card screened by random phase approximation were used for all the clusters. The values utilized from the experiment were a beam energy of 200 kV, semicollection angle of 33 mrad and semiconvergence angle of 27 mrad, taken at the zone axis $[100]$ ($k_x = 1$, $k_y = 0$, $k_z = 0$). A broadening of 0.5 eV was applied to account for the finite resolution in the EELS experiment, which corresponds to the full-width at half-maximum of the zero-loss peak in the EELS spectra.

Data availability

Computer codes used for simulations and data evaluation are available from the sources cited; data in formats other than those presented within this paper are available from the corresponding authors upon request.

References

44. Yan, Z. et al. Growth of high-quality hexagonal ErMnO₃ single crystals by the pressurized floating-zone method. *J. Cryst. Growth* **409**, 75–79 (2015).

45. Jones, L. et al. Smart Align—a new tool for robust non-rigid registration of scanning microscope data. *Adv. Struct. Chem. Imag.* **1**, 8 (2015).
46. Nord, M., Vullum, P. E., MacLaren, I., Tybell, T. & Holmestad, R. Atomap: a new software tool for the automated analysis of atomic resolution images using two-dimensional Gaussian fitting. *Adv. Struct. Chem. Imag.* **3**, 9 (2017).
47. Blöchl, P. E. Projector augmented-wave method. *Phys. Rev. B* **50**, 17953–17979 (1994).
48. Kresse, G. & Furthmüller, J. Efficient iterative schemes for ab initio total-energy calculations using a plane-wave basis set. *Phys. Rev. B* **54**, 11169–11186 (1996).
49. Kresse, G. & Joubert, D. From ultrasoft pseudopotentials to the projector augmented-wave method. *Phys. Rev. B* **59**, 1758–1775 (1999).
50. Medvedeva, J. E., Anisimov, V. I., Korotin, M. A., Mryasov, O. N. & Freeman, A. J. Effect of Coulomb correlation and magnetic ordering on the electronic structure of two hexagonal phases of ferromagnetic YMnO₃. *J. Phys. Condens. Matter* **12**, 4947–4958 (2001).
51. Gibbs, A. S., Knight, K. S. & Lightfoot, P. High-temperature phase transitions of hexagonal YMnO₃. *Phys. Rev. B* **83**, 94111 (2011).
52. Degenhardt, C., Fiebig, M., Fröhlich, D., Lottermoser, T. & Pisarev, R. V. Nonlinear optical spectroscopy of electronic transitions in hexagonal manganites. *Appl. Phys. B* **73**, 139–144 (2001).
53. Perdew, J. P. et al. Restoring the density-gradient expansion for exchange in solids and surfaces. *Phys. Rev. Lett.* **100**, 136406 (2008).
54. Dudarev, S. L., Botton, G. A., Savrasov, S. Y., Humphreys, C. J. & Sutton, A. P. Electron-energy-loss spectra and the structural stability of nickel oxide: an LSDA+U study. *Phys. Rev. B* **57**, 1505–1509 (1998).
55. Murphy, S. T. & Hine, N. D. M. Anisotropic charge screening and supercell size convergence of defect formation energies. *Phys. Rev. B* **87**, 94111 (2013).
56. Rehr, J. J. et al. Ab initio theory and calculations of X-ray spectra. *C.R. Phys.* **10**, 548–559 (2009).

Acknowledgements

We thank T. Grande for fruitful discussions. D.R.S. and S.M.S. were supported by the Research Council of Norway (project no. 231430/F20 and 275139) and acknowledge UNINETT Sigma2 (project no. NN9264K and ntnu243) for providing the computational resources. A.B.M. was supported by NTNU's Enabling technologies: Nanotechnology. The Research Council of Norway is acknowledged for the support to the Norwegian Micro- and Nano-Fabrication Facility, NorFab, project no. 245963/F50 and Norwegian Centre for Transmission Electron Microscopy, NORTEM, Grant no. 197405. A.L.D. was funded by the Norwegian Research Council under project no. 274459 Translate. K.S. acknowledges the support of the European Research Council under the European Union's Horizon 2020 research and innovation program (grant agreement no. 724529), Ministerio de Economía, Industria y Competitividad through grant nos. MAT2016-77100-C2-2-P and SEV-2015-0496, and the Generalitat de Catalunya (grant no. 2017SGR 1506). Z.Y. and E.B. were supported by the US Department of Energy, Office of Science, Basic Energy Sciences, Materials Sciences and Engineering Division under contract no. DE-AC02-05-CH11231 within the Quantum Materials program KC2202. J.A. was supported by the Academy of Finland under project no. 322832. D.M. thanks NTNU for support through the Onsager Fellowship Programme and NTNU Stjerneprogrammet.

Author contributions

D.M.E. coordinated the project and led the scanning probe microscopy work together with T.S.H., both supervised by D.M. A.B.M. conducted the FIB and SEM work under the supervision of A.T.J.v.H. P.E.V., A.T.J.v.H. and A.B.M. conducted the TEM and, together with T.S.H. and D.M.E. analysed the TEM and EELS data. D.R.S. performed the DFT calculations and A.L.D. simulated the EELS spectra supervised by S.M.S. and J.T., respectively. DF-MD calculations were performed by D.G., J.A., D.R.S. and S.M.S. K.S. modelled the defect segregation in electric fields. Z.Y. and E.B. provided the materials and D.G. and J.A. supported the study with image charge and potential alignment correction simulations for charged defects in periodic boundary conditions. D.M.E. and D.M. wrote the manuscript. All the authors discussed the results and contributed to the final version of the manuscript.

Competing interests

The authors declare no competing interests.

Additional information

Supplementary information is available for this paper at <https://doi.org/10.1038/s41563-020-0765-x>.

Correspondence and requests for materials should be addressed to D.M.E. or D.M.